

## Monte Carlo simulations of nanosecond electromagnetic pulse interaction with field-aligned ionospheric plasma density irregularities

M. Kirillin, E. Sergeeva, D. Kurakina, I. Zudin, and M. Gushchin

A.V. Gaponov-Grekhov Institute of Applied Physics of Russian Academy of Sciences,  
46 Ulyanov Street, Nizhny Novgorod 603950, Russia

Corresponding author: Mikhail Kirillin ([kirillin@ipfran.ru](mailto:kirillin@ipfran.ru))

## **Key Points:**

- Monte Carlo model of nanosecond electromagnetic pulse propagation in ionospheric plasma with field-aligned density depletions is developed
  - Frequency dispersion competes with pronounced pathlength dispersion for scattered waves at low frequencies.
  - The effects of density depletions on electromagnetic pulse properties seem weak even for strong plasma density depletions of up to 50%.

1

**17 Abstract**

18 We propose an approach to simulate ultra-wideband (UWB) electromagnetic pulse (EMP)  
19 propagation in ionosphere with magnetic field-aligned irregularities of plasma density based on  
20 Monte Carlo technique. This approach considers propagation of a nanosecond EMP by ray  
21 trajectories in frequency domain, which allows one to analyze the role of scattering effects for  
22 lower and higher harmonics of the pulse. Parameters of the irregularities used in the  
23 simulations are chosen close to those of artificial ionospheric turbulence (AIT) density striations  
24 stimulated by high-frequency (HF) heating facilities. The employed technique provides a  
25 possibility to compare the effects of dispersion and scattering on a waveform of bipolar  
26 nanosecond EMP for various parameters of ionospheric plasma and its disturbances. In the  
27 presence of 10-meter scale, 10-percent level density striations, we show that lower frequencies  
28 are most responsible for the EMP waveform transformation due to the plasma dispersion, and  
29 are scattered away from the initial propagation direction, while higher frequencies experience  
30 minor dispersion and are less scattered. The influence of AIT-type striations on the  
31 straightforward EMP delay and its broadening in time domain is analyzed compared to the EMP  
32 propagation in uniform plasma. Preliminary, the effects of AIT-type striations on EMP  
33 characteristics seem to be weak in the main part of its frequency spectrum, even for strong  
34 (non-realistic) plasma density depletions of up to 50%.

35

**36 1 Introduction**

37 Ultrawideband (UWB) electromagnetic pulses (EMPs) are signals with duration from  
38 tens of picoseconds to several nanoseconds. The frequency spectrum of such signals is very  
39 broad, from about 100 MHz to 10 GHz, since EMPs are as short as one cycle of oscillation of the  
40 electromagnetic field. The development of UWB technology in recent decades (Agee et al.,  
41 1998; Baum, 1992; Nekoogar, 2011) has led to discussion of the possibilities of UWB EMP use  
42 for sounding the ionosphere and building trans-ionospheric radio communication channels  
43 (see, for example, (Soldatov & Terekhin, 2016)). Recently, first experiment of trans-ionospheric  
44 propagation of a nanosecond EMP with its reception onboard a satellite was reported (Zhang et  
45 al., 2024).

46 In this regard, questions inevitably arise about the effect of ionospheric plasma on the  
47 waveform and frequency spectrum of UWB EMP, primarily the effects of dispersion and  
48 scattering on natural and artificial electron density irregularities along the EMP propagation  
49 path. The role of linear dispersion and linear absorption leading to the spreading of the UWB  
50 EMP and a decrease in its amplitude has been extensively studied (see (Arnush, 1975;  
51 Cartwright & Oughstun, 2009; Dvorak, et al, 1997) and references therein), as well as nonlinear  
52 effects for high-power EMPs (Golubev, et al, 2000). Laboratory simulations of UWB EMP  
53 propagation in ionosphere are also being developed under the support of analytical and  
54 numerical models (Es'kin, et al, 2023; Goykhman et al., 2022; Zudin et al., 2024). However, the  
55 effects of ionospheric irregularities on the propagation of UWB EMPs have not been explicitly  
56 studied yet, to our knowledge.

57        Generally, the effect of ionospheric irregularities on the propagation of very-high (VHF,  
 58 30 – 300 MHz), ultra-high (UHF, 300 MHz – 3 GHz), and super-high frequencies (SHF, 3 – 30  
 59 GHz) that overlap the UWB EMPs' frequency spectrum has been actively studied since the  
 60 1970s (Perkins, 1975). In recent years, interest in this problem is driven first of all by ensuring  
 61 the high accuracy of Global Navigation Satellite Systems (GNSS) that use L-band transmission  
 62 channels (see (Aol et al, 2020; Hong et al., 2020; Mrak et al, 2023; Wernik et al, 2003) and  
 63 references therein). To date, models of diffraction and scattering on natural ionospheric  
 64 irregularities with sizes from several kilometers to several meters have been developed that  
 65 allow one to estimate the amplitude and phase scintillations of monochromatic or narrowband  
 66 signals (Carrano et al, 2011; Deshpande et al, 2014; Galiègue et al 2017). These models,  
 67 however, cannot be explicitly applied to analyze the waveforms of UWB EMPs propagating in  
 68 disturbed ionosphere.

69        Artificial ionospheric irregularities (Alls) are a manifestation of artificial ionospheric  
 70 turbulence (AIT) which develops in ionosphere exposed to powerful radio waves (see (Streltsov  
 71 et al., 2018) and references therein). Generation of Alls and their effect on the propagation of  
 72 VHF waves were discovered in early experiments on ionosphere modification (Fialer, 1974).  
 73 Ground-based HF ionosphere heating facilities located at different geographic latitudes (SURA,  
 74 Russia; HAARP, USA; EISCAT-Heating, Norway) (Streltsov et al., 2018) are capable of generating  
 75 the Alls.

76        In scattering of high-frequency waves, the irregularities with scales from meters (and  
 77 even decimeters) to kilometers provide dominating impact. Properties of such Alls were studied  
 78 in sufficient detail from radar scattering after plasma modification by heating facilities, as well  
 79 as from the characteristics of artificial radio emission from ionosphere (Dhillon & Robinson,  
 80 2005; L. Erkhirimov et al, 1988; L. M. Erkhirimov & Mityakov, 1989; Franz et al, 1999; Frolov et  
 81 al, 1997; Grach et al, 2016). Direct measurements of Alls are complicated, however they were  
 82 performed in rocket experiment (Kelley et al., 1995). A simplified model of All system can be  
 83 represented as multiple plasma density depletions up to 10-20% from the background (or  
 84 "striations") oriented parallel to the geomagnetic field, (Franz et al., 1999; Kelley et al., 1995).  
 85 Owing to the pronounced anisotropic mobility of electrons and ions in the geomagnetic field,  
 86 Alls have nearly cylindrical shape. Axial All scale  $l_{\parallel}$  is limited by the thickness of the turbulence  
 87 area and can be as large as several tens of km. Transverse scale of the irregularities  $l_{\perp}$  can be  
 88 about 10 m or even less. Aspect ratio of irregularities  $l_{\parallel}/l_{\perp}$  can be of the order of the ratio of  
 89 frequency of electron collisions with neutral particles to electron gyrofrequency, which  
 90 amounts  $10^{-4}$  in ionospheric F-layer (Robinson, 2002).

91        Our interest in the effect of Alls on the propagation of EMPs in the GHz frequency range  
 92 is because such irregularities can be excited under controlled conditions and be quite small-  
 93 scaled, i.e. of the order of 10 m or less causing considerable scattering of short (meter and  
 94 decimeter) waves. Therefore, the developed models of UWB EMP scattering on ionospheric  
 95 irregularities can in future be verified in active experiments with heating facilities. To date, All-  
 96 caused scintillation of L-band signals has been observed using HAARP (Mahmoudian et al.,  
 97 2018) and EISCAT (Sato et al, 2021) heaters. Moreover, the possibility of generating Alls of very  
 98 small transverse scales of the order of 10 cm, or so-called "super small-scale" (SSS) irregularities  
 99 in the heating experiments is being discussed (Milikh et al, 2008). If density variations in SSS

100 irregularities reach 20-30% (Najmi et al., 2014), such Alls can in principle lead to strong  
101 scattering of GHz signals including UWB EMPs.

102 The frequencies of sub GHz and GHz waves significantly (by several orders of  
103 magnitude) exceed the plasma frequency of the F-layer which is typically below 10 MHz, and  
104 electron collision frequencies (Soldatov & Terekhin, 2016). This leads to a number of  
105 assumptions in a model of UWB EMP interaction with ionospheric irregularities: (1)  
106 approximation of collisionless plasma can be used; (2) the influence of geomagnetic field on the  
107 EMP dispersion can be neglected. Thus, plasma acts as a medium that is transparent to  
108 radiation and does not absorb electromagnetic energy, with an isotropic dielectric constant and  
109 a refractive index close to unity. The irregularities manifest themselves as refractive index  
110 variations (Hunsucker & Hargreaves, 2007), while scattering of GHz waves is determined by the  
111 geometry of irregularities exclusively, i.e. their depth and statistics. However, the three-  
112 dimensional geometry of striations turns out to be quite complex, which complicates  
113 achievement of analytical solutions.

114 To simulate the propagation of GHz waves in ionosphere in the presence of Alls  
115 numerically, a parabolic wave equation (PWE) is used in combination with a series of phase  
116 screens (PSs) that carry information about random distribution of refractive index along the  
117 propagation path. Note that similar numerical approach is widely used to assess the effects of  
118 atmospheric turbulence on electromagnetic wave propagation (Deshpande et al., 2014; Knepp,  
119 2005). Given the limited performance of machine calculations in ionospheric research, two-  
120 dimensional PWE in combination with multiple one-dimensional PSs was previously used to  
121 estimate ionospheric scintillations (Carrano et al., 2011). Due to low dimensionality of the  
122 method, the interpretation and applicability of the results was limited. To represent a realistic  
123 geometry in the case when the EMP propagation path through the ionosphere is several  
124 hundred kilometers and the Alls are obviously three-dimensional, it was proposed to use a  
125 three-dimensional PWE in combination with a series of two-dimensional PSs (Galiègue et al.,  
126 2017), which made it possible to refine the solution at the cost of significant increase of the  
127 calculation time.

128 A good alternative are statistical numerical methods like Monte Carlo (MC) technique  
129 which are actively employed in the wave propagation and energy transport problems. Monte  
130 Carlo method is based on repeated simulation of random ray trajectories and subsequent  
131 statistical processing and analysis of the results obtained. This method is used in various fields  
132 of atmospheric (Marchuk et al., 2013) and ionospheric (Kim, Yoon, Lee, Pullen, & Weed, 2017;  
133 Mountcastle & Martin, 2002; Schlegel, 1973) physics, optics of ocean (Leathers et al, 2004; A.  
134 Luchinin & Kirillin, 2017) and biological tissues (Kirillin et al, 2014; Yan & Fang, 2020). When  
135 applied to the problems of propagation of electromagnetic waves in randomly inhomogeneous  
136 media, the Monte Carlo method allows one to estimate the characteristics of signal amplitudes  
137 and phases after their scattering and absorption in a volume with random dielectric  
138 irregularities. Random medium can be defined by a set of irregularities with known sizes and  
139 refractive index variations, as well as by spatially distributed statistical characteristics of  
140 scattering and absorption. Flexibility in setting the medium properties provides an advantage  
141 for MC technique compared to analytical and semi-analytical modeling that requires  
142 information about the spectral correlation characteristics of the medium which is often

143 available only empirically. Another important point is that MC technique is successfully used to  
 144 solve problems of propagation of ultrashort (similarly, UWB) pulses in randomly  
 145 inhomogeneous media (A. G. Luchinin et al, 2019; A. G. Luchinin & Kirillin, 2021; A. G. Luchinin  
 146 et al, 2024; Sergeeva, Kirillin, & Priezzhev, 2006).

147 The aim of the current paper is to present a methodology based on the Monte Carlo  
 148 technique for modeling the propagation of a nanosecond EMP in the ionospheric plasma  
 149 allowing to account for both the dispersion of the EMP in plasma and the effects associated  
 150 with scattering on small-scaled field-aligned ionospheric plasma irregularities.

151

## 152 **2 Model description**

### 153        2.1     UWB EMP and ionospheric plasma model

154 Let us consider a plane linearly polarized electromagnetic wave with an electric field  
 155  $E_0(\tau = t - z/c)$  which propagates downwards along vertical direction coinciding the z axis  
 156 through a plasma layer of total thickness  $Z_{layer}$ , where c is the speed of light in vacuum. We  
 157 assume the nanosecond EMP of duration  $\tau_0$  is generated at the top of the layer in the plane  $z =$   
 158 0 and has a bipolar shape (Soldatov & Terekhin, 2016):

$$159 \quad E_0(\tau) = H(\eta)H(1 - \eta)\eta(\eta - 0.5)(\eta - 1) \quad (1)$$

160 where  $\eta = \tau/\tau_0$  and  $H(\eta)$  is the Heaviside step function. In frequency domain, the  
 161 shape of the initial EMP is characterized by spectrum  $\tilde{E}_0(f)$ :

$$162 \quad \tilde{E}_0(f) = \int_{-\infty}^{\infty} E_0(\tau) \exp(-j2\pi f\tau) d\tau. \quad (2)$$

163 Complex amplitude  $\tilde{E}(f, z)$  of the signal harmonic the with the frequency  $f$  depends on  
 164 the pathlength  $z$  in uniform plasma as follows:

$$165 \quad \tilde{E}(f, z) = \tilde{E}_0(f) \exp\left(j\frac{z}{c}(1 - n(f))\right), \quad (3)$$

166 where

$$167 \quad n(f) = \sqrt{1 - f_p^2/f^2} \quad (4)$$

168 is the refractive index in plasma with linear plasma frequency  $f_p$ . The latter is defined in  
 169 CGS metric system as  $f_p = \sqrt{\frac{\rho_e e^2}{\pi m_e}}$  where  $e$  and  $m_e$  are the electron charge and mass,  
 170 respectively, and  $\rho_e$  is the electron density (number of electrons per  $\text{cm}^{-3}$ ) in uniform plasma.

171 We suppose the frequency spectrum of a nanosecond EMP propagating in ionosphere  
 172 belongs to the range from tens MHz to several GHz. For frequencies exceeding the plasma  
 173 frequency of the F-layer, we neglect the effects of collisions and typical features of wave  
 174 propagation in the ionosphere located in the geomagnetic field such as the splitting of the  
 175 dielectric constant for O-mode and X-mode, reflection of waves and their thermal dissipation.

176       Figure 1 shows the evolution of EMP shape after its propagation in uniform plasma layer  
 177      with thickness of  $Z_{layer} = 30$  km and plasma frequency  $f_p = 5$  MHz calculated using Eq. (3), as  
 178      well as the its spectrum. Due to dispersion, the shape of UWB EMP undergoes significant  
 179      changes including shape distortion and considerable center of mass displacement. Pulse center  
 180      of mass delay  $\langle \tau \rangle$  and pulse width  $\Delta\tau$  can be estimated numerically as:

$$181 \quad \langle \tau \rangle = \int_0^{\infty} E^2(\tau) \tau d\tau / \int_0^{\infty} E^2(\tau) d\tau, \quad (5)$$

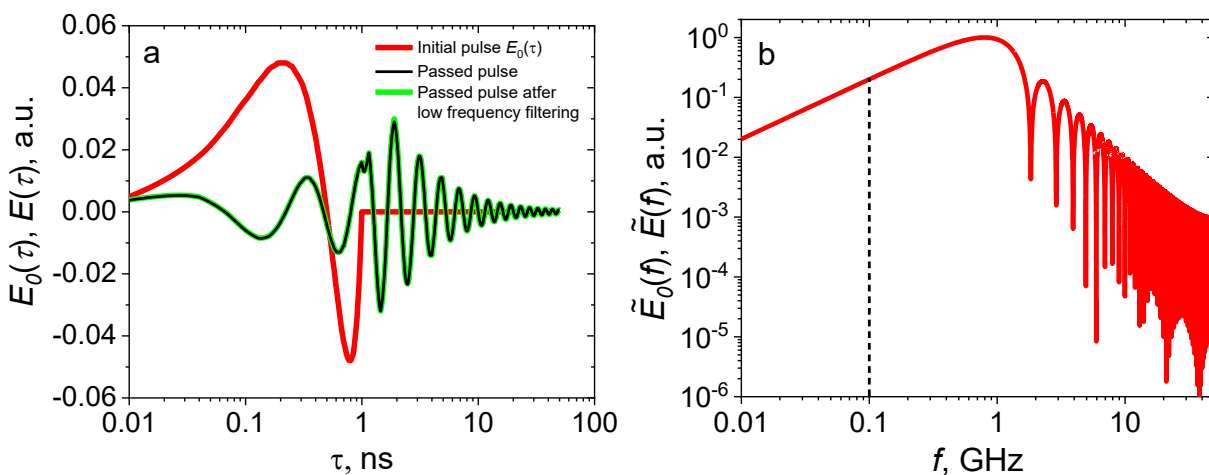
$$182 \quad \Delta\tau = \sqrt{\int_0^{\infty} E^2(\tau) \tau^2 d\tau / \int_0^{\infty} E^2(\tau) d\tau - \langle \tau \rangle^2}. \quad (6)$$

183       For propagation in free space the pulse characteristics are  $\langle \tau \rangle = 0.5\tau_0$  and  
 184       $\Delta\tau \approx 0.29\tau_0$ . Note that even in the absence of Alls, dispersion along the path leads to an  
 185      increase of the pulse delay and width by more than 10 times.

186       We consider the main effect of the pulse-plasma interaction associated with Alls and  
 187      causing difference from propagation in uniform plasma consists in linear scattering of the  
 188      harmonics as they pass through the refractive index irregularities. We characterize the Alls by  
 189      reduced electron density  $\rho_{e,str} = \rho_e (1 - \delta)$ , where  $0 < \delta < 1$  is the relative density depletion  
 190      within the irregularity. For each harmonic  $f$  of the EMP the refractive index  $n_{str}$  inside the  
 191      irregularity can be achieved in the following form:

$$192 \quad n_{str}(f) = \sqrt{1 - f_p^2(1 - \delta)/f^2}, \quad (7)$$

193       and meets the condition  $n(f) < n_{str}(f) < 1$ . Refractive index irregularities due to electron  
 194      density depletion within Alls lead to the EMP scattering, and, consequently, to the additional  
 195      modification of its shape which will be analyzed further within the framework of Monte Carlo  
 196      simulation.



199 **Figure 1.** Shape of initial bipolar UWB EMP with duration of  $\tau_0 = 1$  ns calculated by Eq.(1) and its  
 200 profile after propagation within a uniform plasma layer of the thickness of 30 km with plasma  
 201 frequency  $f_p = 5$  MHz as well as the passed pulse profile after filtering the frequencies below 100  
 202 MHz (**a**); amplitudes of frequency spectrum of initial pulse (**b**).

203        2.2 Monte Carlo technique for modeling the UWB EMP propagation in ionospheric  
 204 plasma with irregularities

205        Among methods that analyze propagation of electromagnetic radiation in a random  
 206 medium, Monte Carlo technique implements the principle of wave-particle duality. A wave is  
 207 presented as a bundle of rays where each ray defines propagation of a small section of the  
 208 wave front. Random trajectory of each ray is simulated as a set of adjacent piecewise linear  
 209 sections. The nodes at the connections of these sections are the points of the ray interaction  
 210 with the scatterers. To consider the wave phenomena, each ray is assigned with the wave  
 211 attributes, such as amplitude and phase, which vary depending on the particular ray trajectory  
 212 in the medium.

213        2.2.1 Frequency domain approach

214        One of the advantages of Monte Carlo method in the problem of UWB EMP propagation  
 215 in ionospheric plasma is its ability to evaluate the effect of Alls in a certain plasma layer on the  
 216 scattering of the ray. In radiation transfer problems, Monte Carlo method can be implemented  
 217 using one of the two most general schemes: (1) a classical scheme with random arrangement of  
 218 scatterers when all scattering events are considered independent, and the position of each  
 219 scatterer is determined at each step based on a priori given scattering and absorption parameters  
 220 of the medium, and (2) a so-called “fixed particle Monte Carlo” (Xiong et al., 2005) in which the  
 221 positions of the scatterers in the medium are defined in advance.

222        In the first scheme, the result of calculation is the average over various possible  
 223 ensembles of scatterers, while the second scheme makes it possible to account for the  
 224 characteristics of radiation propagation within the mean free path in a particular ensemble of  
 225 scatterers. In this study, we used the first classical approach which allows one to obtain a result  
 226 averaged over various ensembles leading to a more general solution compared to a particular  
 227 solution obtained within the second approach.

228        Let us consider the implementation of Monte Carlo algorithm for modeling the ray  
 229 trajectory of  $k$ -th harmonic  $f_k$  from the EMP spectrum defined by Eq. (2) in a layer of ionospheric  
 230 plasma in the presence of Alls. Geomagnetic field aligned cylindrical striations (see Fig.2) are  
 231 considered as a statistical ensemble of scatterers. For simplicity all irregularities are assumed to  
 232 be of the same size but with a varying in-between distance. The input parameters for modeling  
 233 are the harmonic frequency  $f_k$ , plasma frequency  $f_p$  corresponding to the average electron  
 234 density value in the plasma layer, radius  $r$  of a single irregularity, mean ray free path (RFP)  $\langle l \rangle$   
 235 between two adjacent irregularities, depth  $\delta$  of relative electron density depletions within the  
 236 irregularity, and thickness  $Z_{layer}$  of plasma layer containing striations. The properties of EMP  
 237 after passing the plasma layer with striations are analyzed at the layer lower boundary

238  $z = Z_{layer}$ , which is called "detector plane". Detection area is divided into segments with center  
 239 position  $(x_a, y_b)$  and size  $\Delta x \times \Delta y$  where  $\Delta x$  and  $\Delta y$  are dimensions along the corresponding axes.

240 Calculation is based on consequent tracking of N rays which travel from the origin through  
 241 the plasma layer. Let  $i$ -th ray ( $i = 1 \dots N$ ) corresponding to the harmonic with frequency  $f_k$  be  
 242 assigned with a local scalar field:

$$243 \quad E_{i,k}(x, y, z, \tau) = E_{0,k} \cos(2\pi f_k(\tau + z/c) + \varphi_{0,k} - \phi_{i,k}), \quad (8)$$

244 where  $E_{0,k}$  and  $\varphi_{0,k}$  are, respectively, the field amplitude and initial phase of the harmonic in the  
 245 plane  $z = 0$ , and  $\phi_{i,k} = \phi_{i,k}(x, y, z)$  is the phase shift along the pathway in dependence on  
 246 Cartesian coordinates. Local propagation direction is defined by three direction cosines  
 247 ( $\gamma_x, \gamma_y, \gamma_z$ ). Random RFP between the two consecutive scattering events is calculated in  
 248 accordance with semi-empirical concept of single scattering described by the Bouger-Lambert-  
 249 Beer's law. It defines the average intensity  $I(z)$  of the non-scattered plane wave after passing  
 250 the distance  $z$  in the scattering and non-absorbing medium as:

$$251 \quad I(z) = I_0 \exp(-\mu_s z), \quad (9)$$

252 where  $I_0$  is the initial intensity and  $\mu_s$  is the scattering coefficient of the medium which is the  
 253 inverse to the mean free path in the medium:  $\mu_s = 1/\langle l \rangle$ . In this connection, current RFP is  
 254 calculated as follows:

$$255 \quad l = -\ln(\xi)/\langle l \rangle, \quad (10)$$

256 where  $\xi$  is a random value uniformly distributed in the range (0,1].

257 Interaction of the ray with each irregularity is considered within the framework of  
 258 geometric optics approach under the assumption that the transverse size of the irregularity  
 259 significantly exceeds the wavelength for all harmonics of a nanosecond EMP, which limits the  
 260 lowest spectrum frequency. One iteration of a ray tracing cycle includes searching the  
 261 intersection point of the ray trajectory with a cylinder, calculating reflection coefficient  $R_{ref}$  of  
 262 the ray by the cylinder surface in accordance with the Fresnel law. Occurrence of reflection is  
 263 defined by the condition:

$$264 \quad \zeta < R_{ref}, \quad (11)$$

265 where  $\zeta$  is a random value uniformly distributed in the range (0,1]. If condition (11) is met, the  
 266 ray direction changes in accordance with the reflection law, and a new RFP in the external  
 267 medium is generated according to Eq. (10). If condition (11) is violated, refraction of the ray  
 268 occurs. The ray changes its direction according to the Fresnel law and propagates through the  
 269 irregularity to its far boundary, where the reflection test using condition (11) is performed again.  
 270 Simulation of the ray propagation inside the irregularity is performed until a refraction event  
 271 occurs at the cylinder-plasma boundary and the ray exits into the surrounding plasma. In this  
 272 case, a new iteration begins by evaluation of the free path using Eq. (10). Iterations are repeated  
 273 until the ray exits the boundaries of the medium or reaches the detector plane  $z = Z_{layer}$ , which  
 274 coincides with the lower boundary of the layer with irregularities. Output coordinates  $(x_i^{ex}, y_i^{ex})$   
 275 of the  $i$ -th ray in the detection plane are recorded together with the total phase shift  $\phi_{i,k}^{ex}$ :

$$276 \quad \phi_{i,k}^{ex} = 2\pi f_k(n(f_k)L_{p,i} + n_{str}(f_k)L_{str,i})/c, \quad (12)$$

277 where  $L_{p,i}$  is the total ray path in surrounding plasma and  $L_{str,i}$  is the total ray path inside  
278 irregularities.

279 At the final stage, averaging of field oscillations  $E_{i,k}(x^{\text{ex}}, y^{\text{ex}}, \tau) = \tilde{E}_{0,k}(f) \cos(2\pi f_k(\tau +$   
280  $Z_{\text{layer}}/c) + \varphi_{0,k} - \phi_{i,k}^{\text{ex}})$  of all rays reaching the detector plane  $z = Z_{\text{layer}}$  within the segment  
281 ( $x_a, y_b$ ) is performed:

$$282 E_k^{\text{ray}}(x_a, y_b, \tau) = \sum_{i|x_a < x_i^{\text{ex}} < x_a + \Delta x, y_b < y_i^{\text{ex}} < y_b + \Delta y} E_{i,k}(x_i^{\text{ex}}, y_i^{\text{ex}}, Z_{\text{layer}}, \tau) / N. \quad (13)$$

283 It is assumed in Eq. (13) that the output direction of the ray does not change significantly with  
284 respect to the initial direction.

### 285 2.2.2 Frequency scattering map construction

286 To analyze the structure of the EMP in space and time, it is convenient to present the  
287 pulse by a discrete Fourier spectrum with a set of harmonics  $f_k = k/T$  ( $k = 1 \dots N_k$ ):

$$288 \tilde{E}_{0,k} = \frac{1}{T} \int_0^T E_0(\tau) \exp(-j2\pi f_k \tau) d\tau, \quad (14)$$

289 where  $T$  is the pulse record time. Previously described Monte Carlo simulation of ray propagation  
290 can be then performed for each harmonic  $f_k$  followed by summation for all harmonics within the  
291 detector segment ( $x_a, y_b$ ):

$$292 E^{\text{pulse}}(x_a, y_b, \tau) = \\ 293 = \sum_k E_k^{\text{ray}}(x_a, y_b, \tau) = \sum_k \sum_{i|x_a < x_i^{\text{ex}} < x_a + \Delta x, y_b < y_i^{\text{ex}} < y_b + \Delta y} E_{0,i}^k \cos(2\pi f_k(\tau + Z_{\text{layer}}/c) + \varphi_{0,k} - \phi_{i,k}^{\text{ex}}). \quad (15)$$

294 For better visual representation of both effects of scattering and dispersion on the EMP  
295 propagation we propose to construct “frequency scattering maps” similar to construction of a  
296 point spread function. These maps illustrate the deviations of particular frequency harmonics  
297 from straight forward propagation due to scattering, and their arrival to a particular detector  
298 segment ( $x_a, y_b$ ). Such maps can provide a complete picture of the scattering role in ray deflecting  
299 from the straight forward propagation. We constructed the 2D map of minimal  $D_f^{\min}$  and  
300 maximal  $D_f^{\max}$  nonzero frequencies of the pulse discrete spectrum  $\tilde{E}$ :

$$301 D_f^{\min}(x_a, y_b) = \min(f_k | \tilde{E}(x_a, y_b, f_k) > 0) \quad (16)$$

$$302 D_f^{\max}(x_a, y_b) = \max(f_k | \tilde{E}(x_a, y_b, f_k) > 0) \quad (17)$$

303 To our knowledge, it is the first example of this approach in the analysis of spatial-spectral  
304 structure of EMPs in a plasma medium.

### 305 2.2.3 Simulation of plane wave

306 When the source is located at a fairly large distance from the ionospheric layer (significantly  
307 exceeding its thickness), the problem can be considered in the plane wave approximation. It  
308 means that electric field is transversely uniform in the plane of the layer boundary and the  
309 solution obtained for a single ray can be averaged over the detection plane. The solution for a  
310 plane wave can be obtained as follows:

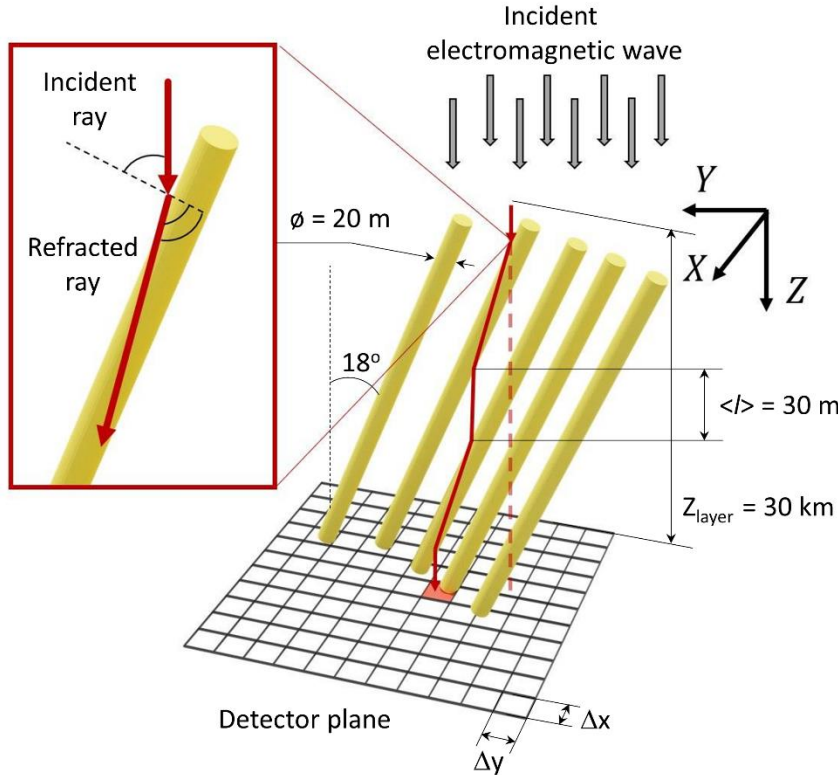
311                    $E^{planar}(\tau) = \sum_{a,b} E^{pulse}(x_a, y_b, \tau) =$

312                    $= \sum_{a,b} \sum_k \sum_{i|x_a < x_i^{\text{ex}} < x_a + \Delta x, y_b < y_i^{\text{ex}} < y_b + \Delta y} E_{0,i}^k \cos(2\pi f_k(\tau + Z_{layer}/c) + \varphi_{0,k} - \phi_{i,k}^{\text{ex}}).$                    (18)

313 In the case of modeling a spherical wave, the effect of the shape of the spherical front can be  
 314 accounted by modeling a set of rays with individual initial directions, initial phase shift and  
 315 coordinates of the entry point into the layer based on an a priori given position of the source.  
 316 Modeling with such initial parameters is carried out separately for each harmonic.

317                   2.3 Problem statement

318 In this study, we considered propagation of an EMP in a layer of ionospheric plasma of  
 319 thickness of  $Z_{layer} = 30$  km containing cylindrical irregularities with radius of  $r = 10$  m (Kelley et  
 320 al., 1995) oriented at an angle of  $\alpha = 18^\circ$  relative to vertical direction which mimic striations  
 321 formed under mid-latitude ionospheric heating conditions as in experiments with SURA heating  
 322 facility. Average RFP between the irregularities was chosen as  $\langle l \rangle = 30$  m. Relative depth of  
 323 electron density depletions within striations varied in the range of  $\delta = 5\% - 50\%$ . The largest  
 324 values of  $\delta$  are hardly realistic, and used in simulations in demonstrative purposes only. Two  
 325 values of electron density in unperturbed plasma were considered corresponding to plasma  
 326 frequencies  $f_p = 5$  MHz and 10 MHz. The pulse duration  $\tau_0$  was assumed to be equal to 1 ns, its  
 327 initial profile in the plane  $z = 0$  was given by Eq.(1). Typical trajectory of a ray propagating in the  
 328 layer with the cylindrical irregularities is shown in Fig. 2. The number of random ray trajectories  
 329 used in the simulations for individual harmonics varied in the range of  $N = 10^5-10^6$ . These values  
 330 were chosen based on preliminary simulations and ensure the invariance of the key  
 331 observables analyzed in this study, such as pulse delay or pulse width, with respect to the  
 332 number of trajectories employed in simulations. Detector plane had the size of 4000 m in X  
 333 direction and 160 m in Y direction, while the size of segments  $\Delta x$  and  $\Delta y$  are 1 m on default, and  
 334 could be specified differently in separate cases.



335

336 **Figure. 2.** Schematic of the model: typical ray trajectory when scattering on ionospheric  
337 irregularities.

### 338 **3 Simulation results**

#### 339 **3.1 Frequency spectrum of a nanosecond pulse in Monte Carlo simulations**

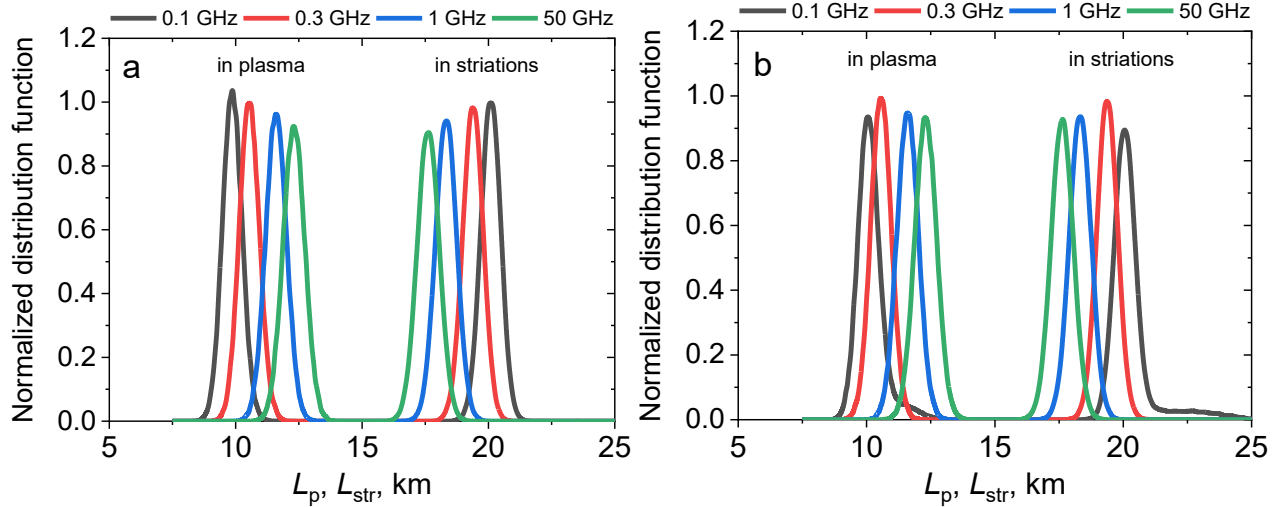
340 First, we have to define the number  $N_k$  of discrete Fourier spectrum harmonics  
341 employed in Monte Carlo simulations of UWB EMP propagating in plasma with striations  
342 according to Eq.(14). The shape of the initial 1-ns pulse given by Eq. (1) is shown in Fig.1 (a)  
343 while analytically calculated harmonic spectrum of the initial pulse and the pulse passing a layer  
344 of uniform plasma with plasma frequency  $f_p = 5 \text{ MHz}$  are shown in Fig.1(b). Lower frequency  
345 limit of 10 MHz is related to the pulse record time of 100 ns, while upper frequency limit of 50  
346 GHz is caused by temporal resolution of the incident pulse which was taken as  $10^{-2} \text{ ns}$ . Total  
347 number of counts used in analytical calculation is  $N_{\text{counts}} = 10^4$  yielding  $N_k = N_{\text{counts}}/2 = 5 \cdot 10^3$   
348 harmonics required to compose the pulse.

349 In Monte Carlo modeling of the ray propagation in plasma with striations, several  
350 assumptions are made which put certain restrictions on the harmonic spectrum of the pulse.  
351 First, the transverse scale of striations is assumed large compared to the particular harmonic  
352 wavelength so that ray optics can be employed. In the case  $r = 10 \text{ m}$  this condition is met for  
353 frequencies not less than 100 MHz which means the first 10 harmonics in the range of 10-100

354 MHz should be withdrawn from the EMP spectrum. Fig.1(a) demonstrates the effect of low-  
 355 frequency filtering on the distortion of the passed pulse shape. The effect is rather minor and it  
 356 is almost negligible in the main body of the pulse in the range of 1-10 ns since the relative loss  
 357 of energy due to the withdrawn harmonics is below 0.2%. Another restriction comes from large  
 358 number of harmonics needed to be simulated for correct reconstruction of a scattered pulse  
 359 shape, which leads to intensive Monte Carlo modeling. In sub-GHz and GHz range the effect of  
 360 the ray refraction is mostly pronounced for lower harmonics while higher harmonics experience  
 361 less refraction. The question is in defining the domain of higher harmonics for which phase  
 362 delay can be evaluated analytically avoiding time-consuming Monte Carlo tracing.

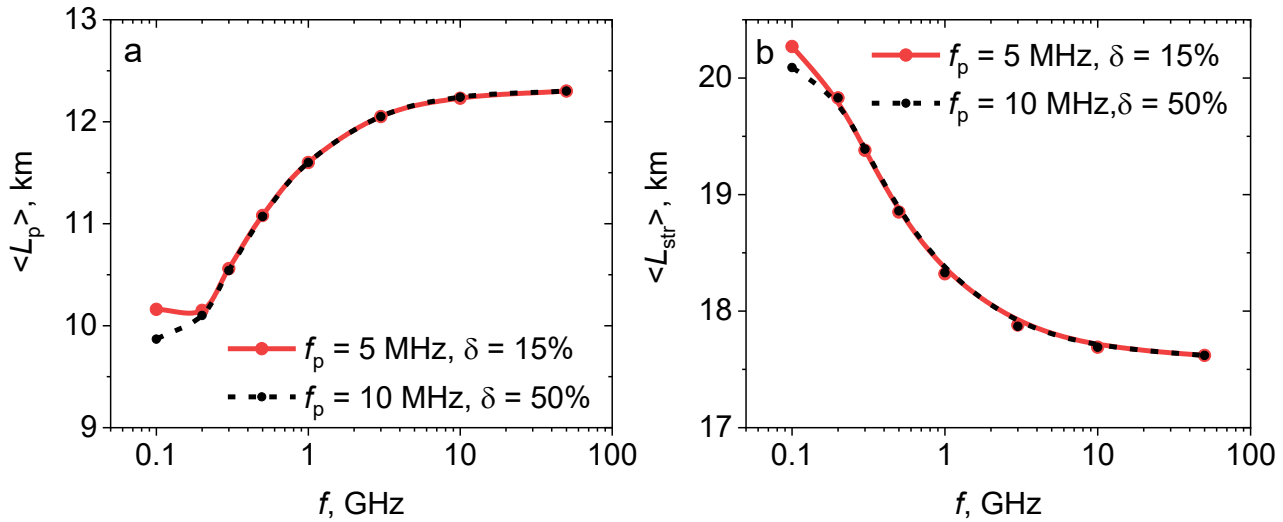
363       3.2 Ray trajectories for different frequency harmonics

364       We considered tracing a single pulsed ray incident on a 30-km-thick layer of plasma in  
 365 the origin ( $x = 0, y = 0, z = 0$ ) and directed along Z axis. We simulated the ray propagation in the  
 366 plasma layer with plasma frequency  $f_p = 5$  MHz containing density irregularities with  $\delta = 15\%$   
 367 which corresponds to some observations (Kelley et al., 1995), as well as the layer with plasma  
 368 frequency  $f_p = 10$  MHz with the irregularities with  $\delta = 50\%$  which is beyond natural conditions  
 369 and is presented as a limiting case. Fig. 3 demonstrates normalized statistical distribution of ray  
 370 pathlengths in plasma ( $L_p$ ) and in striations ( $L_{str}$ ) registered in the whole detector plane  
 371  $z = Z_{layer}$  for four individual EPM harmonics with frequencies of 0.1 GHz, 0.3 GHz, 1 GHz and  
 372 50 GHz. In the case of small  $\delta$  (Fig. 3a) all distributions are Gaussian-shaped with peak position  
 373 and width depending on the harmonic frequency. Lower harmonics are characterized by  
 374 smaller pathlengths in plasma and larger pathlengths within irregularities, as well as by  
 375 narrower width of the distribution. In the case of large  $f_p$  and  $\delta$  (Fig. 3b) the pathlength  
 376 distribution function is asymmetric for lowest harmonics with noticeable contribution of large  
 377 pathlengths both in striations and in the surrounding plasma which describes wandering of the  
 378 ray due to multiple refractions. Dependence of average pathlengths  $\langle L_p \rangle$  and  $\langle L_{str} \rangle$  on the  
 379 frequency for both cases of  $(f_p, \delta)$  is plotted in Fig. 4 for eight harmonics within the range 0.1 –  
 380 50 GHz. Average pathlength increases in plasma with the harmonic frequency (Fig. 4a) while it  
 381 decreases within striations (Fig. 4b) thus showing the lowering effect of refraction in higher  
 382 harmonics. The curves  $\langle L_p \rangle$  and  $\langle L_{str} \rangle$  are almost identical for both cases of  $(f_p, \delta)$  except for  
 383 the region of smallest frequencies where the effect of large-path tail in the distribution for  $f_p =$   
 384 10 MHz and  $\delta = 50\%$  is evident. Asymptotic average pathlength at high frequencies is almost  
 385 the same for weak and strong electron density depletions and amounts about  $\langle L_p \rangle = 12.4$  km  
 386 and  $\langle L_{str} \rangle = 17.6$  km while their sum is equal to the layer thickness  $Z_{layer} = 30$  km.



387

**Figure 3.** Normalized distributions of total pathlength within plasma and striations of the EMP harmonics with the indicated frequencies for the parameters  $f_p = 5$  MHz,  $\delta = 15\%$  (a) and  $f_p = 10$  MHz,  $\delta = 50\%$  (b).



391

**Figure 4.** Average pathlength within background plasma (a) and striations (b) versus frequency for the parameters  $f_p = 5$  MHz,  $\delta = 15\%$  (a) and  $f_p = 10$  MHz,  $\delta = 50\%$  (b).

394

In Fig. 5 scattering maps of minimum  $D_f^{min}$  (Fig. 5a) and maximum  $D_f^{max}$  (Fig. 3b) frequencies from the UWB EMP discrete spectrum are shown. Spatial resolution in the maps is  $\Delta x = \Delta y = 1$  m both in the direction parallel to the projection of the cylinder axis onto the detector plane (Y axis), and orthogonal to it (X axis). The brightest spot in both maps covers central segment around  $(0, 0, Z_{layer})$  point of the detector plane in which all the harmonics of the non-refracted pulse should be observed. In the case of random refraction, lower frequencies deviate from straightforward propagation. The largest shift takes place for smallest

395

396

397

398

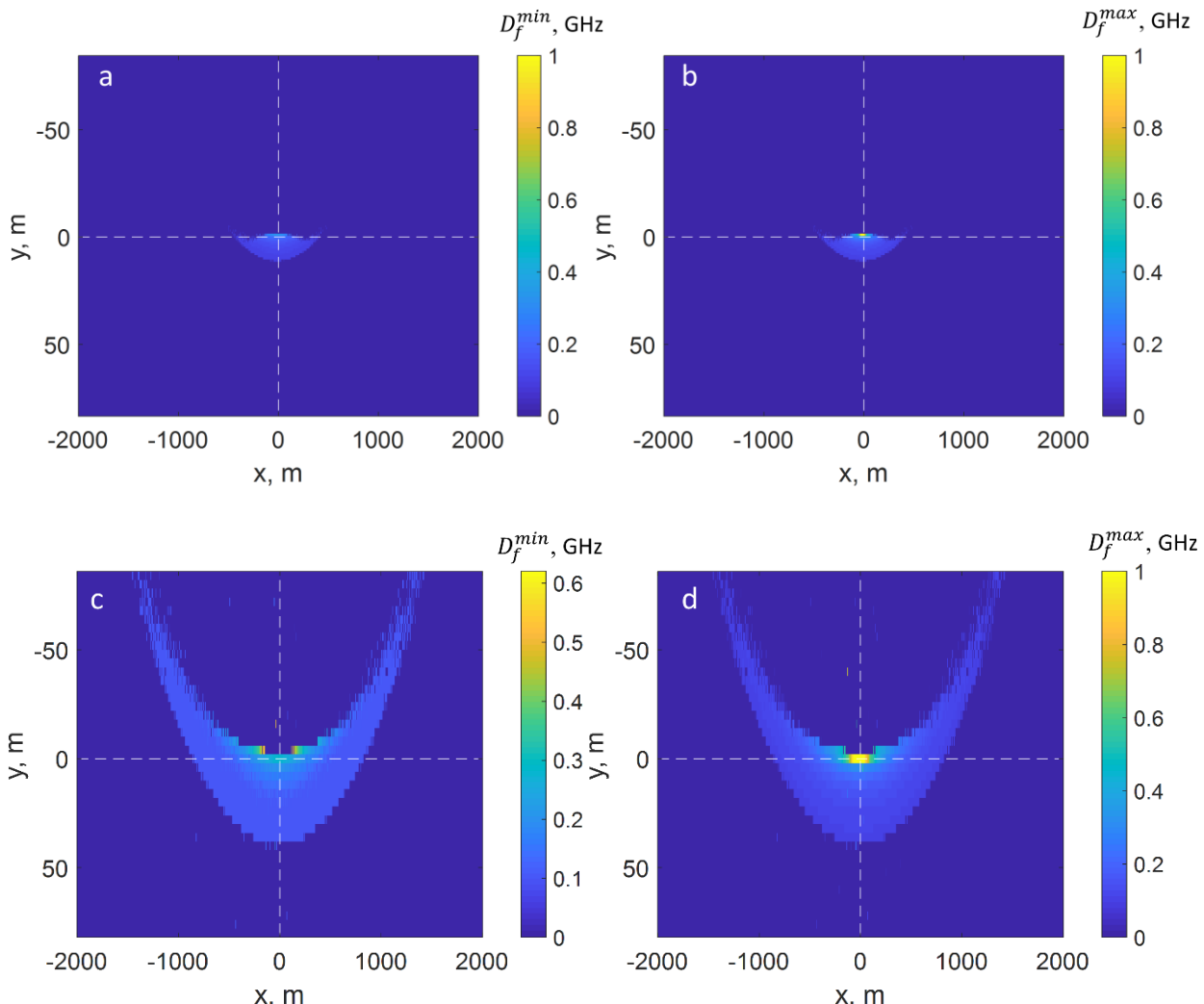
399

400

401

402 frequencies in the spectrum which is related to the maximum difference in the refractive  
 403 indices  $n$  and  $n_{str}$  (see Eq.(4) and Eq.(7)). The anisotropy of the frequency distribution is due to  
 404 the inclination of the irregularities at the angle of  $\alpha = 18^\circ$  with respect to vertical direction.  
 405 Non-uniform displacement is observed along Y axis, i.e., in the direction parallel to the  
 406 projection of the cylinder onto the detector plane, while in the orthogonal direction (along X)  
 407 the distribution is symmetric due to random positions of the striations relative to the initial  
 408 beam direction.

409 The  $D_f^{min}$  map (Fig. 5a) shows that all harmonics with frequencies less than 0.3 GHz  
 410 experience a shift in Y direction, and, hence, the signal in the central segment of the detector,  
 411 associated with the part of the pulse which passes through the medium without scattering, is  
 412 composed of higher harmonics. The entire scattering region for all harmonics covers the range  
 413 of  $\pm 500$  m along X-axis and less than 20 m along Y-axis. According to Fig. 5b, the highest  
 414 harmonics deviate within the limits of one segment along Y direction with size of 1 m, and  
 415 within  $\pm 20$  m along X axis.



416

417

418 **Figure 5.** Scattering maps of minimum  $D_f^{min}$  (**a,c**) and maximum  $D_f^{max}$  (**b,d**) nonzero harmonics  
 419 of EMP discrete spectrum detected after propagation within 30-km-thick plasma layer with  
 420 plasma frequency of  $f_p = 5$  MHz containing Alls with variation of electron density  $\delta = 15\%$  (**a,b**)  
 421 and  $\delta = 50\%$  (**c,d**).  
 422

423 An increase of electron density depletions depth leads to the increased scattering of  
 424 EMP. Figures 3c,d show frequency scattering maps for the case of  $\delta = 50\%$  corresponding to  
 425 intense irregularities. Typical size of the scattering region increases up to 120 m along Y  
 426 direction, and up to  $\pm 3000$  m in X direction.  $D_f^{min}$  map (Fig.5c) shows that higher harmonics (up  
 427 to 0.6 GHz) experience stronger deviation compared to the case of weaker irregularities,  $\delta =$   
 428 15%, (Fig. 5a) where deviation was observed for frequencies below 0.32 GHz only.

429 Detailed analysis of zoomed-in central parts of  $D_f^{max}$  maps (Figs.5b and 5d) shows that  
 430 maximum frequencies which deviate from the central detector segment of the size  $1 \times 1$  m<sup>2</sup> are  
 431 below 10 GHz. This allows limiting the modeling of propagation of different harmonics by  
 432 frequencies in the range of 100 MHz - 10 GHz with the step of 10 MHz. Phase delay of higher  
 433 harmonics with frequencies in the range 10-50 GHz propagating in plasma with striations will  
 434 can be estimated using asymptotic average path lengths  $\langle L_p \rangle$  and  $\langle L_{str} \rangle$  and asymptotic  
 435 dispersion relation used in high-frequency approximation (Soldatov & Terekhin, 2016):

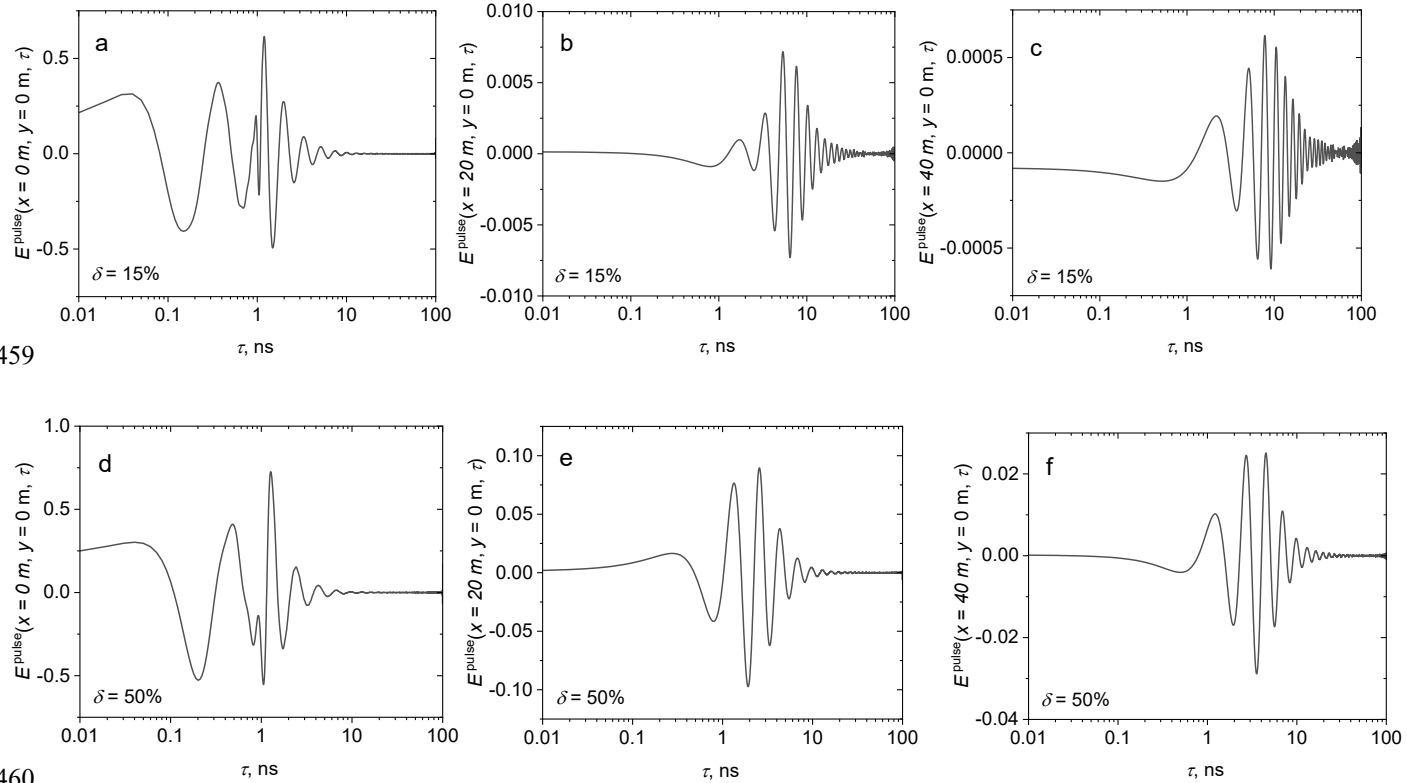
$$436 \phi_k^{\text{ex}} \cong \frac{2\pi f_k}{c} \left( Z_{\text{layer}} - \frac{f_p^2}{2f_k^2} (\langle L_p \rangle + (1 - \delta)\langle L_{str} \rangle) \right) \quad (19)$$

437 The number of harmonics in MC simulations can be thus 5 times reduced, from 5000 to less  
 438 than 1000.

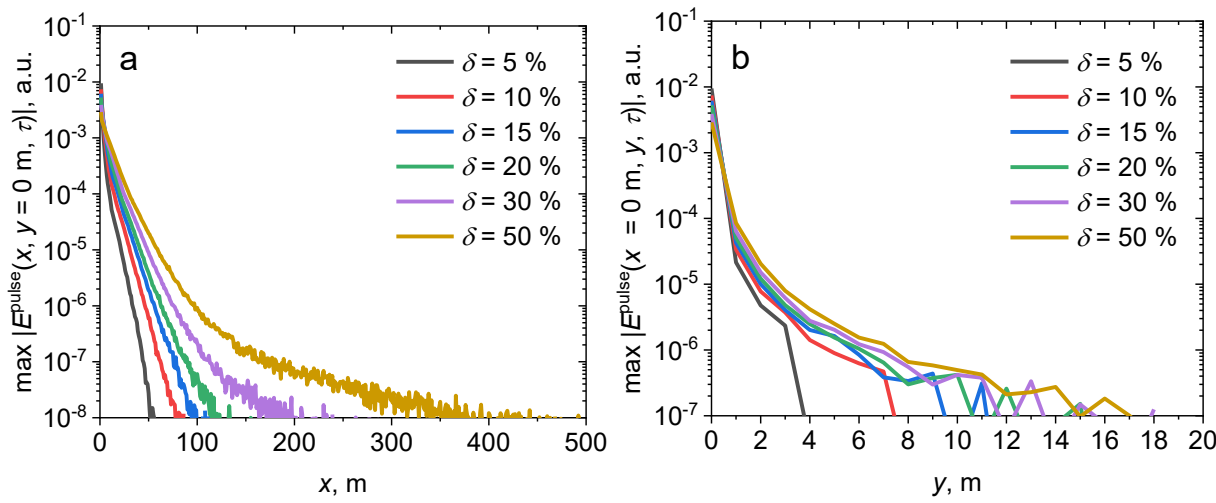
### 439 3.3 Scattered pulse profiles and characteristics

440 Figure 6 shows the waveforms of partial pulsed signals  $E^{\text{pulse}}(x, y, \tau)$  detected by  
 441 different segments of the plane  $z = Z_{\text{layer}}$ . For weaker scattering with  $\delta = 15\%$  the detector  
 442 segments have size  $1 \times 1$  m<sup>2</sup> (Fig. 6a-c); for stronger scattering with  $\delta = 50\%$  the segment size is  
 443  $4 \times 4$  m<sup>2</sup> (Fig. 6d-f). The waveforms are presented in a central segment of the detector plane  
 444 (Fig. 6a, d) and size  $1 \times 1$  m<sup>2</sup> (Fig. 4a) and  $4 \times 4$  m<sup>2</sup> (Fig. 6d) which fully collects the pulse in the case  
 445 of uniform plasma, as well as by the segments of the same size shifted along X axis at distances  
 446 of 20 m (Fig. 6b, e) and 40 m (Fig. 6c, f). The waveforms of partial pulses are composed  
 447 according to Eq.(15) with account for all harmonics arriving at a defined detection segment, and  
 448 are plotted versus the time variable  $\tau = t - Z_{\text{layer}}/c$ . The figure demonstrates that the pulse  
 449 waveform detected in the central segment and therefore composed of a large number of  
 450 harmonics differs considerably from that in the shifted segments where the signal is formed by  
 451 scattered harmonics at low frequencies predominantly. An attenuation of the signal amplitude  
 452 as well as the delay of the pulse center of mass are observed with the increase of the  
 453 transverse shift. Figure 7 presents dependences of the scattered pulse amplitudes  
 454  $\max(|E^{\text{pulse}}(x, y, \tau)|)$  versus the shift along X axis (Fig. 5a) and Y axis (Fig. 7b) for three  
 455 different values of  $\delta = 15, 30$ , and  $50\%$ . Amplitude decays nearly exponentially in X direction for  
 456 up to 100 m (Fig. 7a) with the decay rates that decrease with the increase of  $\delta$ . Slow decay at

457 large distances is most pronounced for high  $\delta$  and is apparently related to deflection due to  
 458 strong multiple refraction.



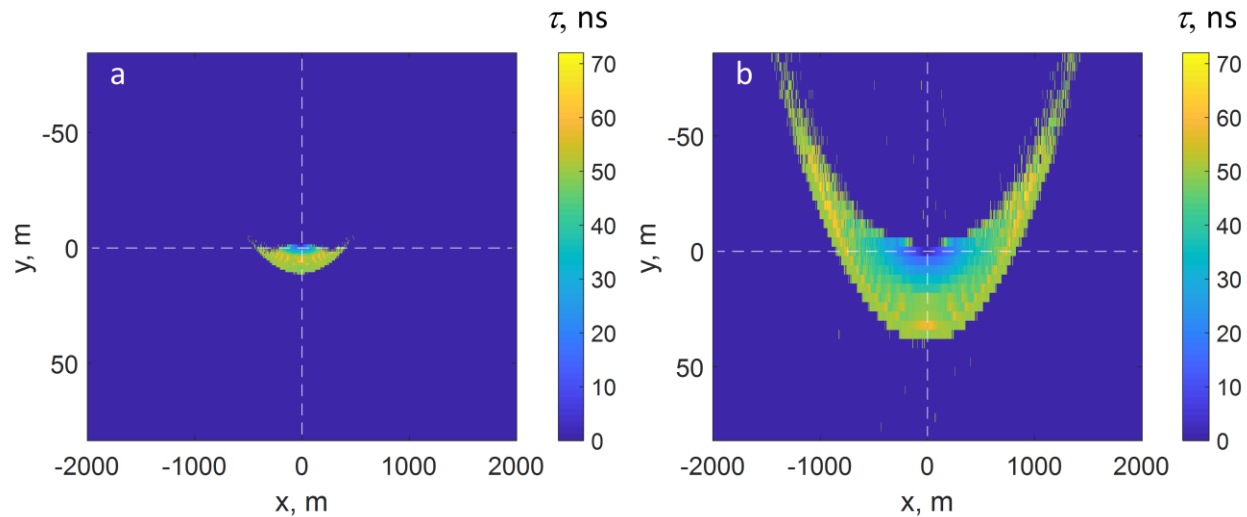
459  
 460 **Figure 6.** Partial pulses  $E^{\text{pulse}}(x, y, \tau)$  detected within the central segment (a,d) and segments  
 461 shifted along X axis for 20 m (b,e) and 40 m (c,f) after the ray propagation in a 30-km-thick plasma  
 462 layer with plasma frequency  $f_p = 5 \text{ MHz}$  in the presence of Alls with  $\delta = 15\%$  (a-c) and  $\delta = 50\%$   
 463 (d-f).  
 464



465

466 **Figure 7.** Dependence of the scattered pulse amplitude max ( $|E^{pulse}(x, y, \tau)|$ ) on transversal  
 467 shift along X axis (**a**) and Y axis (**b**) after propagation in a 30-km-thick plasma layer with plasma  
 468 frequency  $f_p = 5$  MHz in the presence of Alls for various values of electron density depletion  $\delta$ .  
 469

470 Study of average delays of the detected partial pulses is of particular interest. In Fig. 6 maps of  
 471 average delay of partial pulsed signals  $E^{pulse}(x, y, \tau)$  calculated by Eq.(5) are presented for the  
 472 cases of  $\delta = 15\%$  (Fig. 8a) and  $\delta = 50\%$  (Fig. 8b). Note that in the central part of the detection  
 473 plane the case of  $\delta = 15\%$  (Fig. 8a) is characterized by larger delay values compared to the case  
 474 of  $\delta = 50\%$  (Fig. 8b) for a given shift of the detection segment despite stronger scattering in the  
 475 latter case with larger spreading of detected rays. It should be noted that typical delays are of  
 476 few ns in the segments close to the central one, and can reach 72 ns at the periphery. A  
 477 detailed interpretation of this phenomenon will be given in the next section devoted to the  
 478 simulation of a plane wave propagation.



479  
 480 **Figure 8.** Delay maps of detected partial pulses after the ray propagation in a 30-km-thick  
 481 plasma layer with plasma frequency  $f_p = 5$  MHz in the presence of Alls with values of electron  
 482 density fluctuations  $\delta = 15\%$  (**a**) and  $\delta = 50\%$  (**b**).  
 483

484       3.4 Simulation of the propagation of a nanosecond pulse in the plane wave  
 485 approximation

486       To expand the presented results on the case of plane-wave EMP propagation we employ  
 487 the approach described by Eq.(18). For each harmonic, the electric fields detected within the  
 488 whole detector plane  $z = Z_{layer}$  are summarized and then all harmonics are converted into a  
 489 pulse. This simplified approach does not account for the effect of polarization change when  
 490 calculating the net field. Such an assumption was previously made in (Soldatov & Terekhin, 2016)  
 491 in a high-frequency limit. Being convenient, it yields an approximate pulse structure with  
 492 overestimated net amplitudes of the harmonics. In our study, the influence of polarization  
 493 change at the boundaries of striations may be significant for lower frequencies. However,

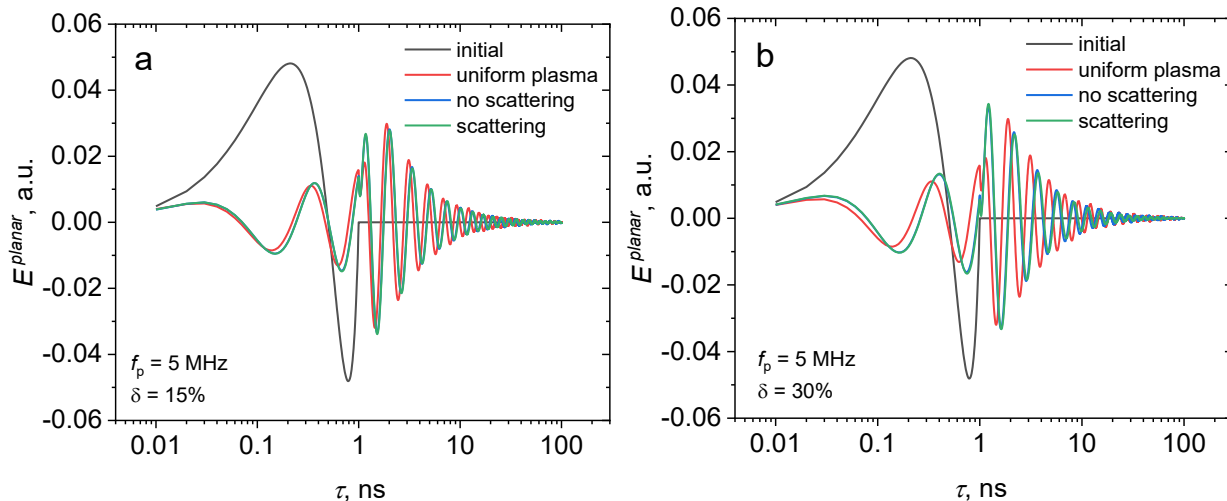
494 preliminary analysis in the frames of geometrical optics shows that depolarization of radiation  
 495 (polarization vector rotation for linearly polarized field) due to scattering on irregularities is of  
 496 the same order as the angular spread of wave vectors  $\theta_k$  of the rays arriving to the observation  
 497 point. This statement can be easily verified by considering the incidence of a beam on a flat  
 498 boundary of two isotropic media. The greatest angle of rotation of the electric field intensity  
 499 vector will be observed in the case of a TM wave, and it will be equal to the angle of rotation of  
 500 the wave vector. In the case of a TE wave, the electric field vector will not rotate at all. The  
 501 magnitude  $\theta_k$ , in its turn, can be evaluated from scattering maps (Fig.5) as  $\Omega_k \approx 0.05 - 0.1$  for  
 502 lower harmonics. Therefore, the effect of polarization change can be omitted at the current step,  
 503 while the results obtained under the stated assumption can be considered as a reference for  
 504 future detailed findings.

505 To demonstrate the effect of random striations on the pulse waveform, we compared two  
 506 models of electron density distribution with depletion. First model is attributed as “no scattering”  
 507 where plasma is considered as a uniform medium with an effective refractive index:

$$508 n_{eff}(f) = \frac{\langle L_p \rangle n(f) + \langle L_{str} \rangle n_{str}(f)}{Z_{layer}} = \frac{1.24n(f) + 1.76n_{str}(f)}{3} \quad (20)$$

509 Propagation of all the harmonics in such medium is considered straight-forward with the  
 510 phase shift calculated in accordance with Eq. 15. Another model is attributed as “scattering”, and  
 511 describes the pulse propagation in plasma with cylindrical irregularities simulated by Monte Carlo  
 512 technique in accordance with Section 2.2.4.

513 The results of modeling the pulse transformation in the plane wave approximation are  
 514 presented in Fig. 9a-c for background plasma frequency  $f_p = 5$  MHz and different values of  $\delta$ . For  
 515 reference, the waveforms of the EMP propagating in uniform plasma (attributed as “uniform  
 516 plasma”) are shown. The presence of irregularities leads to the distortion of the EMP waveform  
 517 which becomes stronger with the increase of  $\delta$ . It is worth noting that the pulse waveforms in  
 518 uniform plasma differ from those in plasma with density distortions both for “no scattering” and  
 519 “scattering” cases. The difference between the latter two cases also grows with the increase of  $\delta$   
 520 value, which is most clearly seen from Fig. 9c for  $\delta = 50\%$ .



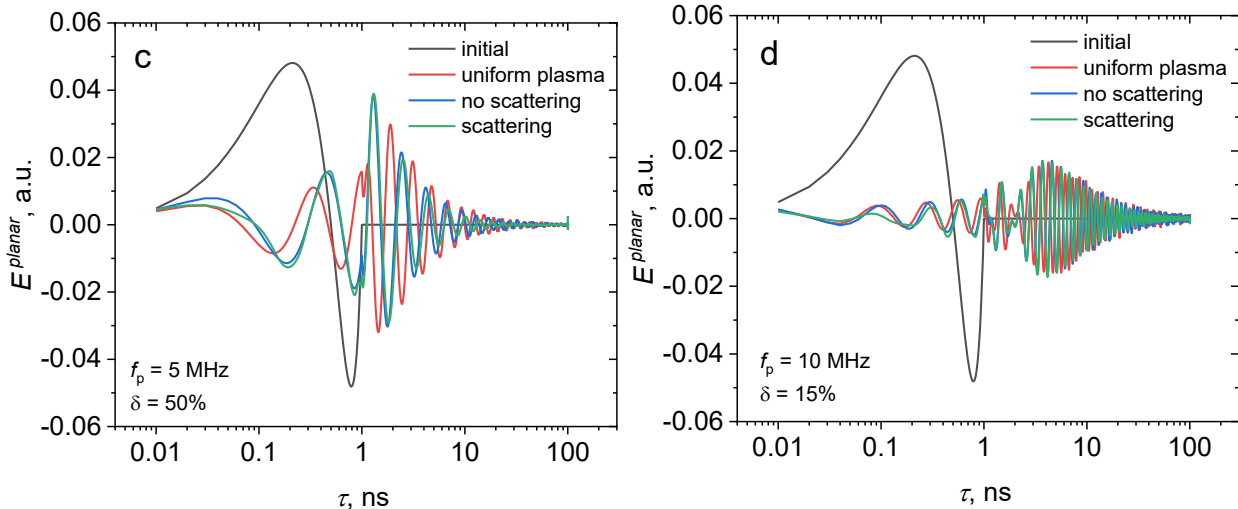
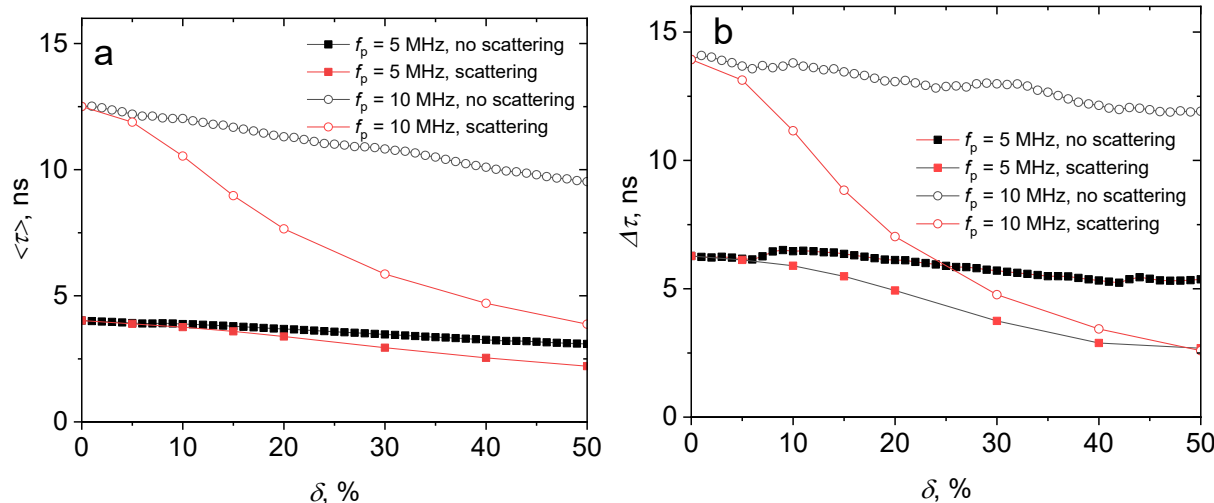


**Figure 9.** Waveforms of a plane wave EMP  $E^{planar}(\tau)$  after propagation in a 30-km-thick plasma layer with background plasma frequency  $f_p = 5$  MHz for uniform plasma (“uniform plasma”), in a medium with effective refractive index depending on electron density fluctuations (“no scattering”), and in plasma with Alls (“scattering”) for electron density fluctuations  $\delta = 15\%$  (a), 30% (b), 50% (c), and  $\delta = 15\%$  with  $f_p = 10$  MHz (d). Initial EMP waveform is given as a reference.

Figure 9d shows the results of the EMP waveform simulations for the case of high background plasma frequency  $f_p = 10$  MHz when the refractive index dispersion is more pronounced. This case is manifested by larger overall delays of the pulse body compared to the case of  $f_p = 5$  MHz. As it seen from comparison of the EMP waveforms in Fig.9a and Fig.9d for the same  $\delta$  but different  $f_p$  values, dispersion has greater impact on the pulse shape compared to scattering effects.

The results of calculating the delays of the EMP center of mass by Eq.(5) are presented in Fig. 10a. Starting point of the plot is a relative delay for a pulse in uniform plasma given as a reference and indicated as “ $\delta = 0$ ”. The figure shows data for both models of density distributions (“no scattering” and “scattering” cases). In “no scattering” model, a delay of the EMP center of mass decreases with the increase of  $\delta$ , which is explained by the fact that refractive index  $n_{str}$  tends to 1 with the growth of  $\delta$ . As a result, average refractive index of the medium also becomes closer to 1 resulting in smaller effect of dispersion. What is worth noting is that the presence of scattering additionally reduces the EMP delay. This is expectable for a plasma-type medium with a refractive index below unity since larger propagation paths of scattered waves give an additional phase delay. As a result, larger propagation paths partly compensate the dispersion. This effect is especially pronounced for smaller frequencies, for which the refractive index  $n$  is smaller, however, scattering is also stronger. Moreover, scattering seems to play a more significant role in dispersion compensation for larger  $\delta$  as compared to “no scattering” case. The effect of scattering can also be illustrated by the delay maps (Fig. 8) which show angular spreading due to scattering. Curves for  $f_p = 5$  MHz and  $f_p = 10$  MHz demonstrate similar systematic decrease of  $\langle \tau \rangle$  in the presence of irregularities compared

551 to the case of EMP propagation in a uniform plasma with effective refractive index. For higher  
 552 value of  $f_p$  a decrease in  $\langle\tau\rangle$  is more apparent.



553  
554

555 Fig. 10. Center of mass delay with respect to EMP propagation in free space (a) and pulse width  
 556 of the pulsed plane wave (b) scattered in a 30-km-thick plasma layer with background plasma  
 557 frequencies  $f_p$  = 5 and 10 MHz in the presence of Alls with different values of  $\delta$ : cases of  
 558 uniform plasma with effective refractive index (no scattering) and plasma with random  
 559 cylindrical irregularities (scattering).

560

561 Dependences of the pulse width  $\Delta\tau$  versus the value of  $\delta$  calculated by Eq.(6) are shown  
 562 in Fig. 10b for both low and high plasma frequencies and demonstrate trends similar to those  
 563 observed for  $\langle\tau\rangle$ . This figure also confirms that the presence of the refractive index irregularities  
 564 can partly compensate dispersion effects and diminish pulse widening. As density depletions  
 565 become deeper with the growth of  $\delta$ , scattering plays more significant role in compensation of  
 566 EMP broadening due to the dispersion.

#### 567 4 Discussion and Conclusions

568 In this study, a methodology based on the Monte Carlo technique was developed for  
 569 modeling the linear propagation of a nanosecond electromagnetic pulse (EMP) in ionospheric  
 570 plasma in the presence of field-aligned depleted density irregularities, which are similar to well-  
 571 known striations stimulated by HF heating experiments. By employing individual ray tracing  
 572 approach, this technique allowed to analyze the effect of scattering by the irregularities on  
 573 lower and higher frequency harmonics of the EMP for different electron densities  
 574 corresponding to typical plasma frequencies from 5 MHz to 10 MHz. Due to the specific  
 575 orientation of the irregularities the scattering is anisotropic and is elongated in the direction  
 576 transversal to irregularities axis projection on the lower boundary of the layer with density  
 577 irregularities. The harmonics below 0.3 GHz deviate from the initial direction for more than 1 m  
 578 within a 30-km path, while harmonics above 10 GHz experience almost no deviation. Simulation

579 of a plane wave propagation demonstrated two competing phenomena affecting the structure  
 580 of the outgoing EMP. On the one hand, the scattering leads to energy loss in the  
 581 straightforward pulse. On the other hand, average refractive index of the medium with the  
 582 irregularities increases with respect to that of basic plasma leading to partial compensation of  
 583 dispersion. The pulse delay and its width decrease with the increase of the electron density  
 584 variation within irregularity indicating stronger role of the former phenomenon.

585 The results obtained are valid within the framework of the simplifying assumptions  
 586 made, which should be recalled.

587 First, the approximation of a collisionless and cold background plasma in a uniform  
 588 magnetic field on a scale of about 30 km is used, which seems to be valid for the conditions of  
 589 propagation of GHz-range signals (including bipolar nanosecond EMPs) in F2-layer of mid-  
 590 latitude ionosphere. Plasma frequencies (5 – 10 MHz) and corresponding background plasma  
 591 densities chosen for simulations ( $\rho_e = 3 \times 10^5 – 10^6 \text{ cm}^{-3}$ ) are quite typical for F2-layer near its  
 592 maximum.

593 Second, the ionospheric irregularities are represented by a system of randomly located,  
 594 field-aligned, cylindrical plasma depletions with sharp boundaries, having the same diameter  
 595 (20 m) and the same level of perturbation of the electron density relative to the background  
 596 value (from 5 to 50 percent). In fact, we are considering irregularities of the smallest diameter  
 597 (according to (Kelly et al., 1995)), the level of density perturbations in which varies from those  
 598 measured in the experiment (approximately 10 percent) to unrealistically high values. The  
 599 length of irregularities (30 km in vertical projection) is chosen to be the maximum possible  
 600 under the conditions of the ionospheric heating experiment. Such irregularity parameters  
 601 should correspond to the strongest scattering effects for GHz-range radiation.

602 Third, the propagation of an EMP in the form of a quasi-plane electromagnetic wave at  
 603 an angle of 18 degrees to the magnetic field direction, which corresponds to vertical  
 604 ionospheric propagation in mid-latitudes, i.e. around the geographical location of the SURA  
 605 heater. The aperture at which the EMP shape is reconstructed in the presence of density  
 606 irregularities is of the order of several kilometers, which is sufficient to collect the  
 607 overwhelming majority of signals scattered by the irregularities in forward direction. Taking into  
 608 account the spherical shape of the EMP front propagating from a finite-sized source may yield  
 609 additional effects, but their discussion is beyond the scope of this paper and will be conducted  
 610 separately.

611 Forth, when simulating the pulse shape after interaction with the irregularities we  
 612 calculate the phases of separate rays and frequency harmonics, but without taking their  
 613 polarization into account.

614 When considering the EMP shape for scattering by irregularities, we excluded frequency  
 615 harmonics below 100 MHz from the analysis. For these harmonics (specifically, from 10 to 100  
 616 MHz), scattering by density striations is no longer described by the geometric optics  
 617 approximation. At the same time, these harmonics might be strongly scattered by irregularities  
 618 and the plasma is transparent for them, therefore, additional grounds are needed to exclude  
 619 them from analysis. Here, on the one hand, it is necessary to point out once again their

extremely small share in the full spectrum of the pulse: less than 0.2 percent in energy. The second significant reason for excluding these harmonics from consideration is the properties of radio wave propagation in the ionosphere with a realistic (non-uniform in height) profile. Indeed, when propagating from the EMP source in the direction of increasing plasma density in the F-layer, spectral harmonics whose frequency is only a few times higher than the maximum plasma frequency will experience strong refraction. Even without irregularities, low-frequency harmonics will drift away from the main high-frequency rays for any finite angle of the ray direction other than strictly vertical propagation. Each act of scattering by an irregularity should lead to a significant deviation of the ray path from the original direction. Furthermore, such harmonics will also experience more pronounced backscattering on irregularities than high-frequency ones. As a result, in addition to their low spectral weight, these harmonics will be further filtered out due to the properties of electromagnetic waves' propagation in ionosphere. As a result, the exclusion of harmonics in the 10-100 MHz range from the analysis of EMPs has, in our opinion, significant physical grounds.

Of course, real density striations in heating experiments are characterized by complex statistics, i.e. they have a spread in length, transverse dimensions, depth, as well as various features of spatial distribution, including clustering. At the same time, from elementary geometric-optical analysis it is obvious that the wider the irregularities and the greater the distance between them, the lesser the scattering effects and their influence on the EMP shape. In this sense, the parameters we selected correspond to the narrowest ( $\sim 10$  m) and deepest density irregularities that can be realized, which lead to the strongest scattering effects. We believe that accounting for the spread of irregularities in transverse dimensions or space positions will only further weaken the influence of irregularities on pulse characteristics, which is already small.

In general, field-aligned density depletions from 10% (a realistic estimate) to 50% (an overestimate) from the background value and a diameter of about 10 m do not have a significant effect on the EMP shape, which is distorted to a much greater extent due to frequency dispersion. Of course, this result requires clarification in further studies – both in terms of taking into account the effects of radiation depolarization on irregularities, and in terms of taking into account the finite radius of curvature of EMP wave front. However, at this stage it is clear that in the approximation of a plane wave of small amplitude propagating in a cold collisionless plasma, one should not expect a significant influence of scattering effects on the amplitude-temporal and spectral characteristics of EMP in the frequency band of about 1 GHz and above.

654

## 655 Acknowledgments

656 The work is supported by Russian Science Foundation, project No. 24-12-00459. The authors  
 657 greatly acknowledge fruitful discussions with Profs. S.M.Grach, V.A.Mironov, A.G Luchinin and  
 658 L.S.Dolin.

## 659 Data Availability Statement

660 The simulations data are available at <https://doi.org/10.5281/zenodo.16687403> [Kirillin 2025].  
 661

## 662 Conflict of Interest

663

664 The authors have no conflicts to disclose.

## 665 References

- 666 Agee, F. J., Baum, C. E., Prather, W. D., Lehr, J. M., O'Loughlin, J. P., Burger, J. W., . . . Hull, J. P. (1998). Ultra-  
 667 wideband transmitter research. *IEEE Transactions on Plasma Science*, 26(3), 860-873.  
 668 AOL, S., Buchert, S., & Jurua, E. (2020). Ionospheric irregularities and scintillations: a direct comparison of in situ  
 669 density observations with ground-based L-band receivers. *Earth, Planets and Space*, 72(1), 164.  
 670 Arnush, D. (1975). Electromagnetic pulse (EMP) propagation through an absorptive and dispersive medium. *IEEE  
 671 Transactions on Antennas and Propagation*, 23(5), 623-626.  
 672 Baum, C. E. (1992). From the electromagnetic pulse to high-power electromagnetics. *Proceedings of the IEEE*,  
 673 80(6), 789-817. doi:10.1109/5.149443  
 674 Carrano, C. S., Groves, K. M., Caton, R. G., Rino, C. L., & Straus, P. R. (2011). Multiple phase screen modeling of  
 675 ionospheric scintillation along radio occultation raypaths. *Radio Science*, 46(06), 1-14.  
 676 Cartwright, N., & Oughstun, K. (2009). Ultrawideband pulse propagation through a homogeneous, isotropic, lossy  
 677 plasma. *Radio Science*, 44(04), 1-11.  
 678 Deshpande, K., Bust, G., Clauer, C., Rino, C., & Carrano, C. (2014). Satellite-beacon Ionospheric-scintillation  
 679 Global Model of the upper Atmosphere (SIGMA) I: High-latitude sensitivity study of the model  
 680 parameters. *Journal of Geophysical Research: Space Physics*, 119(5), 4026-4043.  
 681 Dhillon, R., & Robinson, T. (2005). *Observations of time dependence and aspect sensitivity of regions of enhanced  
 682 UHF backscatter associated with RF heating*. Paper presented at the Annales Geophysicae.  
 683 Dvorak, S. L., Ziolkowski, R. W., & Dudley, D. G. (1997). Ultra-wideband electromagnetic pulse propagation in a  
 684 homogeneous, cold plasma. *Radio Science*, 32(1), 239-250.  
 685 Erukhimov, L., Metelev, S., & Razumov, D. (1988). Diagnostics of ionospheric inhomogeneities with the aid of  
 686 artificial radio emission. *Radiophysics and Quantum Electronics*, 31(11), 928-934.  
 687 Erukhimov, L. M., & Mityakov, N. A. (1989). Modification of the ionosphere as a method of its diagnostics In C. H.  
 688 Liu (Ed.), *World Ionosphere/Thermosphere Study. WITS handbook* (Vol. 2, pp. 267-284). Washington,  
 689 D.C. : National Science Foundation.  
 690 Es'kin, V. A., Korobkov, S. V., Gushchin, M. E., & Kudrin, A. V. (2023). Propagation of an ultrawideband  
 691 electromagnetic pulse along a plasma-filled coaxial line. *IEEE Transactions on Plasma Science*, 51(2),  
 692 374-380.  
 693 Fialer, P. (1974). Field-aligned scattering from a heated region of the ionosphere—Observations at HF and VHF.  
 694 *Radio Science*, 9(11), 923-940.

- 695 Franz, T., Kelley, M., & Gurevich, A. (1999). Radar backscattering from artificial field-aligned irregularities. *Radio*  
 696 *Science*, 34(2), 465-475.
- 697 Frolov, V., Erukhimov, L., Metelev, S., & Sergeev, E. (1997). Temporal behaviour of artificial small-scale  
 698 ionospheric irregularities: Review of experimental results. *Journal of atmospheric and solar-terrestrial*  
 699 *physics*, 59(18), 2317-2333.
- 700 Galiègue, H., Féral, L., & Fabbro, V. (2017). Validity of 2-D electromagnetic approaches to estimate log-amplitude  
 701 and phase variances due to 3-D ionospheric irregularities. *Journal of Geophysical Research: Space Physics*,  
 702 122(1), 1410-1427.
- 703 Golubev, A. I., Syssoeva, T. G., Terekhin, V. A., Tikhonchuk, V. T., & Altgilber, L. (2000). Kinetic model of the  
 704 propagation of intense subnanosecond electromagnetic pulse through the lower atmosphere. *IEEE*  
 705 *Transactions on Plasma Science*, 28(1), 303-311.
- 706 Goykhman, M., Gromov, A., Gundorin, V., Gushchin, M., Zudin, I. Y., Kornishin, S. Y., . . . Loskutov, K. (2022).  
 707 *Concept and practical implementation of a gigantic plasma-filled coaxial line for simulation of the*  
 708 *interaction of electromagnetic pulses with a partially ionized gas medium*. Paper presented at the Doklady  
 709 Physics.
- 710 Grach, S. M., Sergeev, E. N., Mishin, E. V., & Shindin, A. V. (2016) Dynamic properties of ionospheric plasma  
 711 turbulence driven by high-power high-frequency radiowaves. *Phys. Usp.*, 59(11), 1091-1128.  
 712 doi:10.3367/UFNe.2016.07.037868
- 713 Hong, J., Chung, J. K., Kim, Y. H., Park, J., Kwon, H. J., Kim, J. H., . . . Kwak, Y. S. (2020). Characteristics of  
 714 ionospheric irregularities using GNSS scintillation indices measured at Jang Bogo Station, Antarctica  
 715 (74.62 S, 164.22 E). *Space Weather*, 18(10), e2020SW002536.
- 716 Hunsucker, R. D., & Hargreaves, J. K. (2007). *The high-latitude ionosphere and its effects on radio propagation*:  
 717 Cambridge University Press.
- 718 Kelley, M., Arce, T., Salowey, J., Sulzer, M., Armstrong, W., Carter, M., & Duncan, L. (1995). Density depletions  
 719 at the 10-m scale induced by the Arecibo heater. *Journal of Geophysical Research: Space Physics*,  
 720 100(A9), 17367-17376.
- 721 Kim, D., Yoon, M., Lee, J., Pullen, S., & Weed, D. (2017). *Monte Carlo simulation for impact of anomalous*  
 722 *ionospheric gradient on GAST-D GBAS*. Paper presented at the Proceedings of the ION 2017 Pacific PNT  
 723 Meeting.
- 724 Kirillin, M. Y., Farhat, G., Sergeeva, E. A., Kolios, M. C., & Vitkin, A. (2014). Speckle statistics in OCT images:  
 725 Monte Carlo simulations and experimental studies. *Optics letters*, 39(12), 3472-3475.
- 726 Kirillin, M. (2025). Monte Carlo simulations of nanosecond electromagnetic pulse interaction with field-aligned  
 727 ionospheric plasma density irregularities: simulation results [Dataset]. Zenodo.  
 728 <https://doi.org/10.5281/zenodo.16687403>
- 729 Knepp, D. L. (2005). Multiple phase-screen calculation of the temporal behavior of stochastic waves. *Proceedings*  
 730 *of the IEEE*, 71(6), 722-737.
- 731 Leathers, R. A., Downes, T. V., Davis, C. O., & Mobley, C. D. (2004). Monte Carlo radiative transfer simulations  
 732 for ocean optics: a practical guide. *Memorandum report A*, 426624(1).
- 733 Luchinin, A., & Kirillin, M. Y. (2017). Structure of a modulated narrow light beam in seawater: Monte Carlo  
 734 simulation. *Izvestiya, Atmospheric and Oceanic Physics*, 53(2), 242-249.
- 735 Luchinin, A. G., Dolin, L. S., & Kirillin, M. Y. (2019). Time delay and width variation caused by temporal  
 736 dispersion of a complex modulated signal in underwater lidar. *Applied Optics*, 58(18), 5074-5081.
- 737 Luchinin, A. G., & Kirillin, M. Y. (2021). Angular distribution of photon density waves radiance in media with  
 738 different scattering anisotropy. *Applied Optics*, 60(31), 9858-9865.
- 739 Luchinin, A. G., Kirillin, M. Y., & Dolin, L. S. (2024). Evolution of temporal and frequency characteristics of  
 740 spherical photon density waves in scattering media. *Journal of Quantitative Spectroscopy and Radiative*  
 741 *Transfer*, 312, 108799.
- 742 Mahmoudian, A., Scales, W., Taylor, S., Morton, Y., Bernhardt, P., Briczinski, S., & Ghader, S. (2018). Artificial  
 743 ionospheric GPS phase scintillation excited during high-power radiowave modulation of the ionosphere.  
 744 *Radio Science*, 53(6), 775-789.
- 745 Marchuk, G. I., Mikhailov, G. A., Nazareliev, M., Darbinjan, R. A., Kargin, B. A., & Elepov, B. S. (2013). *The*  
 746 *Monte Carlo methods in atmospheric optics* (Vol. 12): Springer.
- 747 Milikh, G., Gurevich, A., Zybin, K., & Secan, J. (2008). Perturbations of GPS signals by the ionospheric  
 748 irregularities generated due to HF-heating at triple of electron gyrofrequency. *Geophysical Research*  
 749 *Letters*, 35(22).

- 750 Mountcastle, P. D., & Martin, M. D. (2002). Monte Carlo simulation of ionospheric scintillation. *Proceedings of the*  
751 *2002 IEEE Radar Conference* (IEEE Cat. No. 02CH37322), 350 – 355.
- 752 Mrak, S., Coster, A. J., Groves, K., & Nikoukar, R. (2023). Ground-based infrastructure for monitoring and  
753 characterizing intermediate-scale ionospheric irregularities at mid-latitudes. *Frontiers in Astronomy and*  
754 *Space Sciences*, 10, 1091340.
- 755 Najmi, A., Milikh, G., Secan, J., Chiang, K., Psiaki, M., Bernhardt, P., . . . Papadopoulos, K. (2014). Generation and  
756 detection of super small striations by F region HF heating. *Journal of Geophysical Research: Space*  
757 *Physics*, 119(7), 6000-6011.
- 758 Nekoogar, F. (2011). *Ultra-Wideband Communications: Fundamentals and Applications Fundamentals and*  
759 *Applications*: Prentice Hall Press.
- 760 Perkins, F. (1975). Ionospheric irregularities. *Reviews of Geophysics*, 13(3), 884-884.
- 761 Robinson, T. (2002). Effects of multiple scatter on the propagation and absorption of electromagnetic waves in a  
762 field-aligned-striated cold magneto-plasma: implications for ionospheric modification experiments.  
*Annales Geophysicae*, 20, 41-55.
- 763 Sato, H., Rietveld, M. T., & Jakowski, N. (2021). GLONASS observation of artificial field-aligned plasma  
764 irregularities near magnetic zenith during EISCAT HF experiment. *Geophysical Research Letters*, 48(4),  
765 e2020GL091673.
- 766 Schlegel, K. (1973). Monte Carlo simulation of a model ionosphere—II. Energy flow and energy dissipation.  
*Journal of Atmospheric and Terrestrial Physics*, 35(3), 415-424.
- 767 Sergeeva, E. A., Kirillin, M. Y., & Priezzhev, A. V. e. (2006). Propagation of a femtosecond pulse in a scattering  
768 medium: theoretical analysis and numerical simulation. *Quantum Electronics*, 36(11), 1023.
- 769 Soldatov, A., & Terekhin, V. (2016). Propagation of an ultrawideband electromagnetic signal in ionospheric plasma.  
*Plasma Physics Reports*, 42(10), 970-977.
- 770 Streltsov, A., Berthelier, J.-J., Chernyshov, A., Frolov, V., Honary, F., Kosch, M., . . . Rietveld, M. (2018). Past,  
771 present and future of active radio frequency experiments in space. *Space Science Reviews*, 214(8), 118.
- 772 Wernik, A., Secan, J., & Fremouw, E. (2003). Ionospheric irregularities and scintillation. *Advances in Space*  
773 *Research*, 31(4), 971-981.
- 774 Xiong, G., Xue, P., Wu, J., Miao, Q., Wang, R., & Ji, L. (2005). Particle-fixed Monte Carlo model for optical  
775 coherence tomography. *Optics express*, 13(6), 2182-2195.
- 776 Yan, S., & Fang, Q. (2020). Hybrid mesh and voxel based Monte Carlo algorithm for accurate and efficient photon  
777 transport modeling in complex bio-tissues. *Biomedical Optics Express*, 11(11), 6262-6270.
- 778 Zhang, T., Li, Z., Duan, C., Wang, L., Wei, Y., Li, K., . . . Cao, B. (2024). Design of a High-Power Nanosecond  
779 Electromagnetic Pulse Radiation System for Verifying Spaceborne Detectors. *Sensors (Basel, Switzerland)*,  
780 24(19), 6406.
- 781 Zudin, I., Gushchin, M., Korobkov, S., Strikovskiy, A., Katkov, A., Kochedykov, V., & Petrova, I. (2024). Transformation of the Shape and Spectrum of an Ultrawideband Electromagnetic Pulse in a “Gigantic”  
782 Coaxial Line Filled with Magnetized Plasma. *Applied Sciences*, 14(2), 705.
- 783
- 784
- 785
- 786
- 787
- 788